

Radiative corrections to the parity-violating spin asymmetry

D.H.Jakubassa-Amundsen¹ and X.Roca-Maza^{2,3,4,5*}

¹*Mathematics Institute, University of Munich, Theresienstrasse 39, 80333 Munich, Germany*

²*Departament de Física Quàntica i Astrofísica, Martí i Franqués, 1, 08028 Barcelona, Spain*

³*Dipartimento di Fisica “Aldo Pontremoli”, Università degli Studi di Milano, 20133 Milano, Italy*

⁴*INFN, Sezione di Milano, 20133 Milano, Italy and*

⁵*Institut de Ciències del Cosmos, Universitat de Barcelona, Martí i Franqués, 1, 08028 Barcelona, Spain*

(Dated: July 22, 2025)

The parity-violating spin asymmetry A_{pv} for elastic electron scattering from spin-zero nuclei, together with its QED corrections, is evaluated non-perturbatively within the phase-shift analysis. Dispersion corrections, taking into account low-lying transient nuclear excitations, are estimated with the help of the lowest-order γZ box diagrams. Collision energies between 5 – 500 MeV are considered, and results are provided for the ^{12}C and ^{208}Pb target nuclei. In addition, we have evaluated A_{pv} at GeV energies and small scattering angles –relevant for the Pb Radius Experiment (PREx)– revealing that the low-lying nuclear excited states give no measurable dispersive contribution. However, they are important at lower energies and backward angles.

1. INTRODUCTION

High-precision measurements of the parity-violating spin asymmetry A_{pv} at GeV collision energies have become feasible during the recent years [1–3], improving earlier experiments [4]. Since A_{pv} depends strongly on the neutron ground-state distribution and on the Weinberg mixing angle, it serves to extract the target neutron skin [5–7], but also provides information on the weak neutral current couplings and the weak charge radius [8–10]. For this application of A_{pv} it is mandatory for theory to take into account any possible corrections as precisely as possible. Here we consider the radiative corrections from vacuum polarization and the vertex plus self-energy correction, as well as from dispersion, based on the excitation of low-lying nuclear states. Dispersion estimates are usually obtained from the γZ box diagrams [11, 12] and are used to correct the weak charge Q_{w} which enters into the normalization of the weak potential A_{w} [5, 13]. Also the universal radiative corrections, estimated in Born approximation, are included in the modification of Q_{w} [11, 14]. An exact calculation of dispersion involves the sum over all transient excited nuclear states. Several approximations have been in use. The earliest one is the closure approximation where all nuclear excitations are taken at the same energy, which lies preferably in the giant dipole resonance region [15]. For lower collision energies it is more adequate to consider explicitly the most collective excited states with small angular momentum and extending up to about 30 MeV [16]. A different approach, applicable for higher collision energies above the pion production threshold (135 MeV), relies on the relation between dispersion, respectively the forward nuclear Compton amplitude, and the experimental photoproduction cross section [17–19]. An application to the γZ box

diagram can be found in [12, 20]. Alternatively, the relation between dispersion and the structure functions from parity-violating deep inelastic scattering can be employed [11].

The present work is aimed at an interpretation of future precision experiments at the MESA facility on the parity-violating asymmetry for low-energy electron scattering [21]. Hence the QED effects are treated nonperturbatively by expressing them in terms of potentials [22–24] which are included in the Dirac equation for the electronic scattering states. Moreover, in the γZ box diagrams, the low-lying nuclear excitations are considered explicitly in terms of their transition densities as obtained from nuclear Energy Density Functionals [25–27]. By inserting the dispersion correction directly into the differential scattering cross section, one is independent of the widely used Born representation of A_{pv} .

The paper is organized as follows: Sec. 2 describes the theory for A_{pv} and its radiative corrections. Results for the ^{12}C and ^{208}Pb target nuclei are presented in Sec. 3. Concluding remarks follow in Sec. 4. Atomic units ($\hbar = m_e = e = 1$) are used unless indicated otherwise.

2. THEORY

In this section the theory for A_{pv} is shortly recapitulated, followed by the treatment of the QED corrections. Finally dispersion is considered to lowest order.

2.1. Parity-violating spin asymmetry

For collision energies well above 10 MeV, the electron mass m_e can usually be neglected. Hence the electrons polarized longitudinally, i.e. parallel (+) or antiparallel (–) to their direction of motion, are described by the helicity eigenstates ψ_+ , respectively ψ_- , which are solutions

*Electronic address: dj@math.lmu.de; Electronic address: xavier.roca.maza@fq.ub.es

to the Dirac equation

$$[-ic\boldsymbol{\alpha}\nabla + V(r) \pm A_w(r)] \psi_{\pm}(\mathbf{r}) = E \psi_{\pm}(\mathbf{r}), \quad (2.1)$$

where, to start with, $V(r) = V_T(r)$ is taken as the Coulombic nuclear target potential. The weak potential $A_w(r)$ is related to the weak density $\varrho_w(r)$ by means of [5]

$$A_w(r) = \frac{G_F c}{2\sqrt{2}} \varrho_w(r), \quad (2.2)$$

where $G_F = 1.1663 \times 10^{-5} [\text{MeV}^{-2}] = 4.545 \times 10^{-7} [\text{a.u.}]$ is the Fermi coupling constant. The parity-violating (or 'weak') spin asymmetry is obtained from the relative cross section difference,

$$A_{\text{pv}} = \frac{d\sigma/d\Omega(+)-d\sigma/d\Omega(-)}{d\sigma/d\Omega(+)+d\sigma/d\Omega(-)}, \quad (2.3)$$

where the differential scattering cross section for the helicity (+) and (-) states is given by

$$\frac{d\sigma_{\text{coul}}}{d\Omega}(\pm) = \frac{|\mathbf{k}_f|}{|\mathbf{k}_i|} \frac{1}{f_{\text{rec}}} \sum_{\sigma_f} |A_{fi}^{\text{coul}}(\psi_{\pm})|^2. \quad (2.4)$$

We have attached the superscript 'coul' to the scattering amplitude A_{fi} to indicate that the potential $V(r)$ used in the Dirac equation is solely the Coulombic nuclear potential. The momenta of the incoming and scattered electron are denoted by k_i and k_f , respectively, σ_f is the final spin polarization and f_{rec} is a recoil factor close to unity [28].

2.2. QED corrections

The scattering amplitude A_{fi}^{QED} , which includes the QED effects, is obtained from the wavefunctions ψ_{\pm} which are solutions to (2.1) in the modified potential

$$V(r) = V_T(r) + V_{\text{vac}}(r) + V_{\text{vs}}(r). \quad (2.5)$$

The potential V_{vac} for vacuum polarization is taken to be the Uehling potential as parametrized in [29]. The potential V_{vs} for the vertex plus self-energy (vs) correction is defined in terms of the integral representation [23],

$$V_{\text{vs}}(r) = -\frac{2Z}{\pi} \int_0^{\infty} d|\mathbf{q}| \frac{\sin(|\mathbf{q}|r)}{|\mathbf{q}|r} F_L(|\mathbf{q}|) F_1^{\text{vs}}(-q^2), \quad (2.6)$$

where Z is the nuclear charge number and $q^2 = (E_i - E_f)^2/c^2 - \mathbf{q}^2$ with $\mathbf{q} = \mathbf{k}_i - \mathbf{k}_f$ is the squared 4-momentum transfer to the nucleus. E_i and E_f are, respectively, the total energies of the incoming and scattered electron. F_L is the nuclear ground-state charge form factor and F_1^{vs} is the electric form factor describing the vs correction in the first-order Born approximation [30, 31].

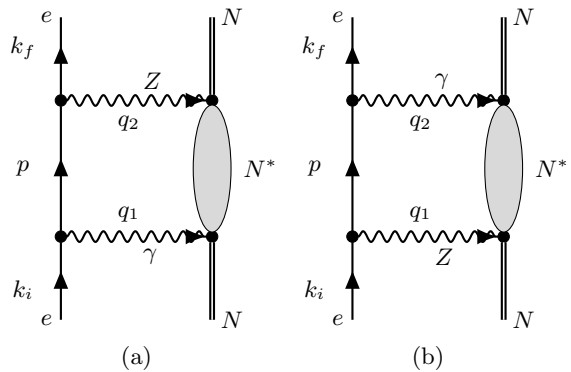


FIG. 1: Feynman box diagrams for dispersion. Diagram (a) describes the electron (e) nucleus (N) coupling by a photon (γ) with momentum q_1 and subsequently by a Z boson with momentum q_2 . N^* indicates the excitation of the nucleus N while k_i and k_f are the momenta of the incoming and scattered electron. In diagram (b), the order is reversed.

In concord with (2.4), the differential cross section is given by

$$\frac{d\sigma^{\text{QED}}}{d\Omega}(\pm) = \frac{|\mathbf{k}_f|}{|\mathbf{k}_i|} \frac{1}{f_{\text{rec}}} \sum_{\sigma_f} |A_{fi}^{\text{QED}}(\psi_{\pm})|^2. \quad (2.7)$$

The corresponding parity-violating spin asymmetry, termed $A_{\text{pv}}^{\text{QED}}$, is defined by (2.3), with $d\sigma/d\Omega$ replaced by $d\sigma^{\text{QED}}/d\Omega$.

2.3. Dispersion effects

In lowest-order Born approximation, dispersion is calculated from the two Feynman box diagrams shown in Fig. 1, involving one virtual photon and one Z boson. The contributions from the crossed-box diagrams are found to be small, and also the seagull diagrams can be disregarded according to [15].

The initial and final electronic helicity eigenstates are described by plane waves,

$$\psi_{i,\pm}^{(0)} = u_{k_i}^{(\pm)}$$

$$\psi_{f,+}^{(0)} = \cos \frac{\theta}{2} u_{k_f}^{(+)} + \sin \frac{\theta}{2} u_{k_f}^{(-)} \quad (2.8)$$

$$\psi_{f,-}^{(0)} = -\sin \frac{\theta}{2} u_{k_f}^{(+)} + \cos \frac{\theta}{2} u_{k_f}^{(-)},$$

where $u_k^{(\pm)}$ are plane-wave 4-spinors (with the prefactor $\sqrt{(E+c^2)/(2E)}$), retaining the electron mass) and θ is the scattering angle. A coordinate system is chosen where the z -axis is along \mathbf{k}_i , while \mathbf{k}_f lies in the (x, z) -plane. The cross section with inclusion of the dispersion

amplitude A_{fi}^{box} , as calculated from the box diagrams of Fig. 1, is to lowest order given by

$$\begin{aligned} \frac{d\sigma^{\text{box}}}{d\Omega}(\pm) &= \frac{|\mathbf{k}_f|}{|\mathbf{k}_i|} \frac{1}{f_{\text{rec}}} \sum_{\sigma_f} [|A_{fi}^{\text{coul}}(\psi_{\pm})|^2 \\ &+ 2 \text{Re} \{ A_{fi}^{\text{coul}*}(\psi_{\pm}) A_{fi}^{\text{box}}(\psi_{\pm}^{(0)}) \}], \end{aligned} \quad (2.9)$$

$$\begin{aligned} A_{fi}^{\text{box}}(\psi_{\pm}^{(0)}) &= 2\sqrt{\frac{E_i E_f}{c^2}} \sum_{L, \omega_L} \left[M_{fi}^{Z\gamma}(L, \omega_L, \pm) \right. \\ &\left. + M_{fi}^{\gamma Z}(L, \omega_L, \pm) \right], \end{aligned}$$

where L is the angular momentum and ω_L the corresponding energy of the transient nuclear excited state.

The transition matrix element $M_{fi}^{Z\gamma}$ corresponds to the first and $M_{fi}^{\gamma Z}$ to the second Feynman diagram of Fig. 1. The evaluation of $M_{fi}^{Z\gamma}$ and $M_{fi}^{\gamma Z}$ proceeds as in the case of the beam-normal spin asymmetry [16], but with the substitution of the first, respectively, the second, virtual photon by the Z boson. This implies the replacement of the photon propagator by the Z -boson propagator,

$$\frac{g^{\mu\nu}}{q^2 + i\epsilon} \mapsto \frac{g^{\mu\nu} - q^\mu q^\nu / (M_z^2 c^2)}{q^2 - M_z^2 c^2 + i\epsilon} \approx \frac{g^{\mu\nu}}{-M_z^2 c^2}, \quad \mu, \nu = 0-3, \quad (2.10)$$

where $g^{\mu\nu}$ is the metric tensor, and the momentum dependence is eliminated due to the large mass $M_z \gg q/c$ of the Z boson.

One also has to substitute the electron- γ vertex by the electron- Z vertex, dictated by the Standard Model [32],

$$\frac{ie}{\sqrt{c}} [\bar{u}_f \gamma_\mu u_i] \mapsto -\frac{i}{4} g_z [\bar{u}_f \gamma_\mu (4 \sin^2 \theta_w - 1 + \gamma_5) u_i], \quad (2.11)$$

where γ_μ are Dirac matrices and $\gamma_5 = \begin{pmatrix} 0 & 1 \\ 1 & 0 \end{pmatrix}$ is the 4×4 chirality matrix. We have introduced the weak coupling constant g_z of the Z boson,

$$g_z = \frac{g_w}{\cos \theta_w}, \quad g_w = \sqrt{\frac{8M_w^2 c^4 G_F}{\sqrt{2}}}, \quad (2.12)$$

where g_w is the coupling constant of the W boson, θ_w is the Weinberg mixing angle ($\sin^2 \theta_w = 0.23146$ [32]) and $M_w c^2$ is the rest energy of the W boson.

Likewise, the γ -nucleus vertex has to be replaced by the Z -nucleus vertex,

$$-\frac{ie}{\sqrt{c}} (\bar{\phi}_n \gamma_0 J_{\text{em}}^\mu \phi_n) \mapsto -\frac{i}{4} g_z (\bar{\phi}_n \gamma_0 J_w^\mu \phi_n), \quad (2.13)$$

where J_{em} is the electromagnetic, J_w the weak transition current and ϕ_n a nuclear state.

Extending the isospin rotation model, derived on the quark level, which relates the proton (P) and neutron

(N) matrix elements of the weak current to the corresponding ones of the electromagnetic current (neglecting the strange-quark contribution) [12, 33],

$$(P | J_w^\mu | P) = (1 - 4 \sin^2 \theta_w) (P | J_{\text{em}}^\mu | P) - (N | J_{\text{em}}^\mu | N)$$

$$(N | J_w^\mu | N) = (1 - 4 \sin^2 \theta_w) (N | J_{\text{em}}^\mu | N) - (P | J_{\text{em}}^\mu | P), \quad (2.14)$$

where the coefficients are given by the Standard Model, to arbitrary nuclei with neutron number $N \neq Z$, one has

$$\begin{aligned} (\bar{\phi}_n \gamma_0 J_w^\mu \phi_n) &= Z (P | J_w^\mu | P) + N (N | J_w^\mu | N) \\ &= (1 - \frac{N}{Z} - 4 \sin^2 \theta_w) (\phi_P | J_{\text{em}}^\mu | \phi_P) \\ &+ (1 - \frac{Z}{N} - 4 \sin^2 \theta_w) (\phi_N | J_{\text{em}}^\mu | \phi_N). \end{aligned} \quad (2.15)$$

In this expression, ϕ_P denotes the proton part and ϕ_N the neutron part of the nuclear wavefunction ϕ_n , and we have interpreted $(P | J_{\text{em}}^\mu | P) = \frac{1}{Z} (\phi_P | J_{\text{em}}^\mu | \phi_P)$ and $(N | J_{\text{em}}^\mu | N) = \frac{1}{N} (\phi_N | J_{\text{em}}^\mu | \phi_N)$.

For isospin-zero nuclei like ^{12}C , the Z -nucleus vertex simplifies to

$$\begin{aligned} &-\frac{i}{4} g_z (\bar{\phi}_n \gamma_0 J_w^\mu \phi_n) \\ &= i g_z \sin^2 \theta_w [(\phi_P | J_{\text{em}}^\mu | \phi_P) + (\phi_N | J_{\text{em}}^\mu | \phi_N)]. \end{aligned} \quad (2.16)$$

Let us first consider the diagram (a) of Fig. 1. With the above modifications of the two-photon case, the transition matrix element $M_{fi}^{Z\gamma}$ of (2.9) can be written in the following way (see [16]),

$$\begin{aligned} M_{fi}^{Z\gamma}(L, \omega_L, \pm) &= -\frac{4\pi}{(2\pi)^3} \frac{e^2}{c} \left(\frac{g_z}{4}\right)^2 \\ &\times \int d\mathbf{p} \frac{1}{(-M_z^2 c^2)} \frac{1}{q_1^2 + i\epsilon} \sum_{\mu\nu} t_{\mu\nu}^{Z\gamma}(\pm) \sum_M (T_n^{Z\gamma})^{\mu\nu}, \end{aligned} \quad (2.17)$$

where $q_1 = k_i - p$ and the sum runs over the magnetic quantum number M of the nuclear state with angular momentum L .

The electronic transition matrix element $t_{\mu\nu}^{Z\gamma}$ reads, considering (2.11) and helicity conservation,

$$\begin{aligned} t_{\mu\nu}^{Z\gamma}(\pm) &= c \left[\psi_{f,\pm}^{(0)} (4 \sin^2 \theta_w - 1 + \gamma_5) \gamma_0 \gamma_\mu \right. \\ &\times \left. \frac{E_p + c\boldsymbol{\alpha}\mathbf{p} + \gamma_0 c^2}{E_p^2 - p^2 c^2 - c^4 + i\epsilon} \gamma_0 \gamma_\nu \psi_{i,\pm}^{(0)} \right], \end{aligned} \quad (2.18)$$

where $E_p \approx E_i - \omega_L$ is the energy of the electron in its intermediate state. It should be noted that the electron

mass is retained here. However, the spin-flip contributions (i.e. $\psi_{i,\pm} \rightarrow \psi_{f,\mp}$) are mostly negligibly small, except at the lowest energies or at the backmost angles. The latter feature is well-known from Coulombic scattering where the longitudinal spin asymmetry A_L drops from +1 to -1 when $\theta \rightarrow 180^\circ$ [34]. For example, for ^{12}C at 55 MeV and 175° , the spin-flip contributions to the relative spin asymmetry change amount to 3%.

Generalizing (2.15) to inelastic nuclear transitions from the ground state $|0\rangle$ to an excited state $|n\rangle$ (characterized by the quantum numbers L and M), the matrix element $(T_n^{Z\gamma})^{\mu\nu}$ for this transient excitation is given by

$$(T_n^{Z\gamma})^{\mu\nu} = \langle 0|J_w^\mu(\mathbf{q}_2)|n\rangle \langle n|J_P^\nu(\mathbf{q}_1)|0\rangle,$$

$$J_w^\mu(\mathbf{q}) = \left(1 - \frac{N}{Z} - 4\sin^2\theta_w\right) J_P^\mu(\mathbf{q}) \quad (2.19)$$

$$+ \left(1 - \frac{Z}{N} - 4\sin^2\theta_w\right) J_N^\mu(\mathbf{q}),$$

where J_w^μ is the weak transition density, constructed from the superposition of the proton (J_P^μ) and neutron (J_N^μ) parts of the charge ($\mu = 0$) and magnetic ($\mu = 1, 2, 3$) transition densities of the target nucleus. Its matrix elements can be expressed in terms of weak transition form factors [16],

$$\langle n|J_w^\mu(\mathbf{q})|0\rangle \quad (2.20)$$

$$= \begin{cases} 4\pi i^L F_L^{c,w}(|\mathbf{q}|) Y_{LM}^*(\hat{\mathbf{q}}), & \mu = 0 \\ -4\pi i \sum_{\lambda=L\pm 1} i^\lambda F_{L\lambda}^{te,w}(|\mathbf{q}|) (\mathbf{Y}_{L\lambda}^{M*}(\hat{\mathbf{q}}))^m, & \mu = m \end{cases}$$

with $m = 1, 2, 3$ and Y_{LM} , respectively $\mathbf{Y}_{L\lambda}^M$, a spherical harmonic function and a vector spherical harmonics. The weak form factors $F_L^{c,w}$ and $F_{L,L\pm 1}^{te,w}$ are the Fourier transforms of the weak transition densities, which are constructed from the same linear superposition of proton and neutron transition densities as used in (2.19). The photon-induced matrix elements $\langle n|J_P^\nu|0\rangle$ are also obtained from (2.20) by replacing, respectively, the weak form factors with the charge (F_L^c) and the transverse electric ($F_{L\lambda}^{te}$) form factors.

Making use of gauge invariance, the photon propagator is decomposed in the usual way [35],

$$\frac{g^{\mu\nu}}{q^2 + i\epsilon} = -\frac{1}{q^2} \delta_{\mu 0} \delta_{\nu 0} - \frac{\delta_{mn} - \hat{q}^m \hat{q}^n}{q^2 + i\epsilon} \delta_{\mu m} \delta_{\nu n}, \quad m, n = 1-3, \quad (2.21)$$

where \hat{q}^m is the m -th component of the unit vector in direction of \mathbf{q} . Therefore one can write

$$\sum_{\mu\nu=0}^3 t_{\mu\nu}^{Z\gamma} \frac{1}{q_1^2 + i\epsilon} (T_n^{Z\gamma})^{\mu\nu} = \sum_{\mu\nu=0}^3 t_{\mu\nu}^{Z\gamma} \sum_{\varrho=0}^3 g^{\mu\varrho}$$

$$\times \sum_{\tau=0}^3 \frac{g^{\nu\tau}}{q_1^2 + i\epsilon} (T_n^{Z\gamma})_{\varrho\tau}$$

$$= -\frac{1}{q_1^2} \sum_{\mu=0}^3 (t^{Z\gamma})_\mu^0 (T_n^{Z\gamma})_{\mu 0} - \frac{1}{q_1^2 + i\epsilon} \quad (2.22)$$

$$\times \left[\sum_{m=1}^3 \sum_{\mu=0}^3 (t^{Z\gamma})_\mu^m \left((T_n^{Z\gamma})_{\mu m} - \hat{q}_1^m \sum_{k=1}^3 \hat{q}_1^k (T_n^{Z\gamma})_{\mu k} \right) \right].$$

For the integration over the electronic intermediate states in (2.17), the variable \mathbf{p} is shifted to $\mathbf{p}' = \mathbf{p} - \mathbf{k}_i = -\mathbf{q}_1$, such that the denominator $1/q_1^2$ in the first term of (2.22) is cancelled. This means that the evaluation of $M_{fi}^{Z\gamma}$ is done with the same techniques that are applied to the transition amplitudes M_{fi}^c and M_{fi}^{te1} of the two-photon box diagram. In contrast, the innermost integral (over the azimuthal angle of \mathbf{p}) does not contain any singularity. This speeds up convergence and avoids the logarithmic singularity which occurs in the cross section for the two-photon box diagram.

Nevertheless, the absence of $1/(q_2^2 + i\epsilon)$ with $q_2 = p - k_f$ in the integrand leads to a poorer convergence with respect to the upper integration limit p_{\max} of the radial integral, which therefore relies solely on the vanishing of the transition form factors at large momentum transfers.

For diagram (b) of Fig. 1, the transition matrix element $M_{fi}^{\gamma Z}$ is obtained from (2.17) by replacing $t_{\mu\nu}^{Z\gamma}$ and $(T_n^{Z\gamma})^{\mu\nu}$ with $t_{\mu\nu}^{\gamma Z}$ and $(T_n^{\gamma Z})^{\mu\nu}$, respectively, as well as changing the denominator $q_1^2 + i\epsilon$ to $q_2^2 + i\epsilon$.

Decomposing $g^{\mu\varrho}/(q_2^2 + i\epsilon)$ according to (2.21), one arrives at an expression corresponding to (2.22),

$$\sum_{\mu\nu=0}^3 t_{\mu\nu}^{\gamma Z} \frac{1}{q_2^2 + i\epsilon} (T_n^{\gamma Z})^{\mu\nu} = -\frac{1}{q_2^2} \sum_{\nu=0}^3 (t^{\gamma Z})_\nu^0 (T_n^{\gamma Z})_{0\nu}$$

$$- \frac{1}{q_2^2 + i\epsilon} \left[\sum_{m=1}^3 \sum_{\nu=0}^3 (t^{\gamma Z})_m^\nu ((T_n^{\gamma Z})_{m\nu} \right. \quad (2.23)$$

$$\left. - \hat{q}_2^m \sum_{k=1}^3 \hat{q}_2^k (T_n^{\gamma Z})_{k\nu} \right].$$

The nuclear transition matrix element reads

$$(T_n^{\gamma Z})^{\mu\nu} = \langle 0|J_P^\mu(\mathbf{q}_2)|n\rangle \langle n|J_w^\nu(\mathbf{q}_1)|0\rangle, \quad (2.24)$$

while the electronic matrix element $t_{\mu\nu}^{\gamma Z}$ is calculated from (2.18) by moving the factor $(4\sin^2\theta_w - 1 + \gamma_5)$ to the right, adjacent to $\psi_{i,\pm}^{(0)}$ according to (2.11). For this second diagram the integration variable \mathbf{p} is shifted to $\mathbf{p}' = \mathbf{p} - \mathbf{k}_f = \mathbf{q}_2$. Therefore, also here, the same techniques can be used as for the evaluation of the transition amplitudes M_{fi}^{te2} and M_{fi}^{te3} of the two-photon box diagram [16].

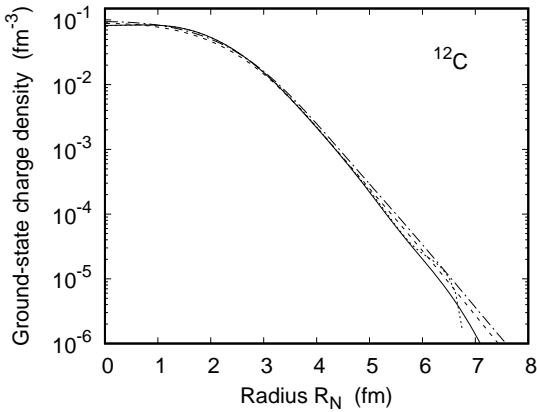


FIG. 2: Ground-state charge density ϱ_0 of ^{12}C as function of the distance R_N from the nuclear center. Shown are the Gaussian parametrization (—), the Fourier-Bessel fit (·····) and the result from the nuclear model (-·-·-). Included is the absolute value of the weak density ϱ_w (- - -).

3. RESULTS

In this section we present estimates for the parity-violating spin asymmetry and its radiative corrections. To this aim, the Dirac equation is solved with the help of the Fortran code RADIAL [36]. The spin asymmetry modification ΔA_{pv} is defined by

$$\Delta A_{\text{pv}}^{\text{QED}/\text{box}} = A_{\text{pv}}^{\text{QED}/\text{box}} - A_{\text{pv}}, \quad (3.1)$$

where the synonym A_{pv} denotes the spin asymmetry relating to the Coulombic field, i.e. $V(r) = V_T(r)$ in (2.1). For low collision energies or small scattering angles (when A_{pv} keeps well away from zero), it is reasonable to define the relative spin asymmetry change dA_{pv} ,

$$dA_{\text{pv}} = \frac{\Delta A_{\text{pv}}}{A_{\text{pv}}}. \quad (3.2)$$

For dispersion, the relative spin asymmetry changes $dA_{\text{pv}}^{\text{box}}(L, \omega_L)$, pertaining to a given excited nuclear state with angular momentum L and excitation energy ω_L , are additive,

$$dA_{\text{pv}}^{\text{box}} \approx \sum_{L, \omega_L} dA_{\text{pv}}^{\text{box}}(L, \omega_L). \quad (3.3)$$

This additivity is based on the fact that the relative cross section changes by dispersion are small (well below 10^{-6}).

When the two kinds of radiative corrections are of comparable size, they have to be combined. However, a simple addition is not possible since the relative cross section change $\Delta\sigma^{\text{QED}} = \frac{d\sigma^{\text{QED}}}{d\Omega} / \frac{d\sigma^{\text{conl}}}{d\Omega} - 1$ by the QED effects (excluding soft bremsstrahlung) is in general large (up to -20%). Therefore the weak spin asymmetry which includes the radiative corrections has to be calculated from

$$A_{\text{pv}}^{\text{box}+\text{QED}} \approx A_{\text{pv}}^{\text{QED}} + A_{\text{pv}} \cdot dA_{\text{pv}}^{\text{box}} \frac{1}{1 + \Delta\sigma^{\text{QED}}}, \quad (3.4)$$

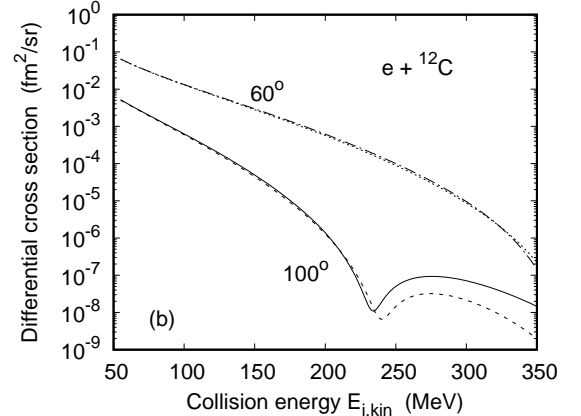
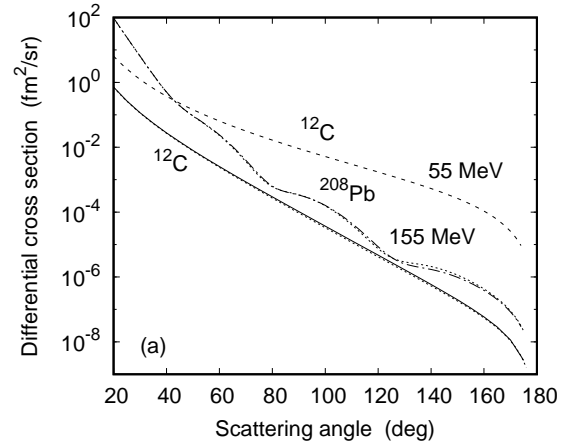


FIG. 3: Differential cross section $\frac{d\sigma^{\text{conl}}}{d\Omega}$ for unpolarized electrons (a) scattering from ^{12}C at 55 MeV (- - -) and at 155 MeV (-·-·-), as well as from ^{208}Pb at 155 MeV (·····) as function of the scattering angle θ , using a Gaussian charge distribution. Included are the results from the numerical ϱ_0 for 155 MeV (·····). (b) scattering from ^{12}C at $\theta = 60^\circ$ (-·-·-) and 100° (—) as function of collision energy $E_{i,\text{kin}}$, using a Gaussian ϱ_0 . Included are the results from the numerical ϱ_0 for 60° (·····) and 100° (- - -).

and correspondingly its relative change,

$$dA_{\text{pv}}^{\text{box}+\text{QED}} \approx dA_{\text{pv}}^{\text{QED}} + dA_{\text{pv}}^{\text{box}} \cdot \frac{1}{1 + \Delta\sigma^{\text{QED}}}. \quad (3.5)$$

Two spin-zero nuclei, ^{12}C and ^{208}Pb , are considered in what follows.

3.1. The ^{12}C nucleus

For the ground-state charge distribution ϱ_0 , from which the nuclear potential V_T is generated, three different prescriptions were considered: a parametrization with a sum of Gaussians [40], a Fourier-Bessel (FB) parametrization [40], both obtained from a fit to elastic scattering data, and a numerical ϱ_0 calculated from the

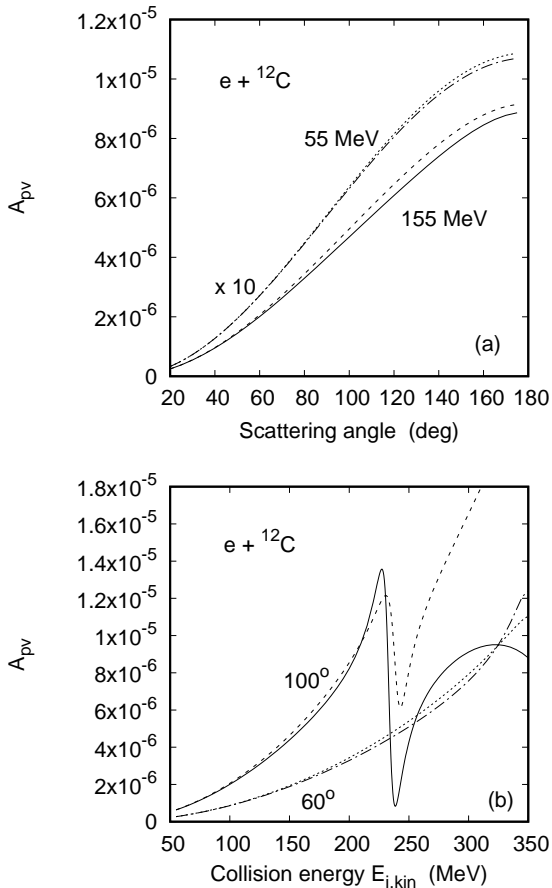


FIG. 4: Parity-violating asymmetry A_{pv} for electron scattering from ^{12}C (a) at 55 MeV (---, multiplied by a factor of 10) and 155 MeV (—) as function of scattering angle θ and (b) at 60° (---) and 100° (—) as function of collision energy, using a Gaussian charge distribution. The results from the numerical charge density are also shown, at 55 MeV (·····, multiplied by 10) and 155 MeV (----) in (a) and at 60° (·····) and 100° (----) in (b).

SkM* nuclear model [37]. They are displayed in Fig. 2. The shapes of the FB and the Gaussian parametrization are nearly identical (up to 5.5 fm), with a minimum near $R_N = 0$. However, there are considerable deviations between these two densities and the theoretical one.

Fig. 3 shows the angular and energy distribution of the differential cross section for the elastic scattering of unpolarized electrons, as obtained by means of the phase-shift analysis [41]. At low energies (Fig. 3a) the difference arising from the choice of the Gaussian ϱ_0 and the theoretical ϱ_0 is small, mostly below 10% at 155 MeV and less ($\lesssim 3\%$) at 55 MeV. However, in the vicinity of the first diffraction minimum (at a momentum transfer $q \approx 1.84 \text{ fm}^{-1}$, Fig. 3b) these deviations are formidable, the more so, the higher the collision energy. The above momentum transfer corresponds to a mean electron-nucleus distance $R_N \approx q^{-1} = 0.54 \text{ fm}$ where the respective choices of ϱ_0

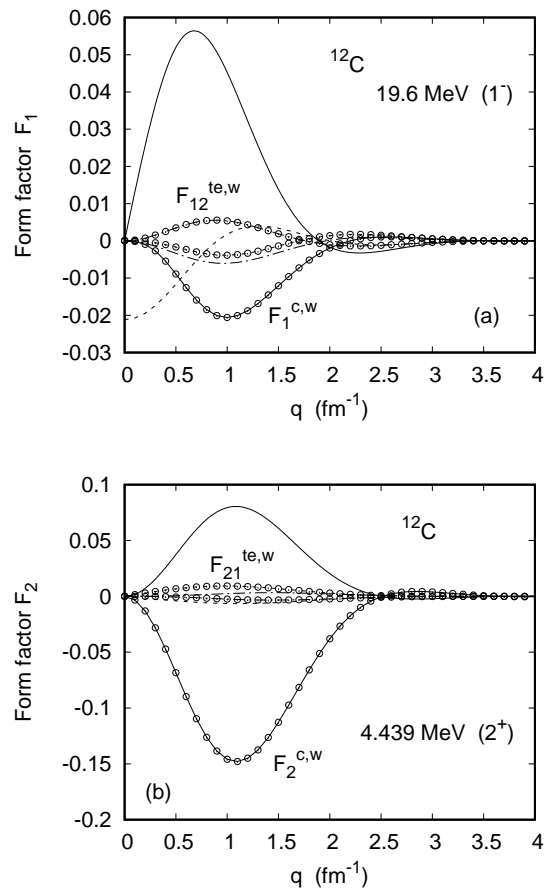


FIG. 5: ^{12}C form factors as function of momentum transfer (a) for the isovector 1^- state at 19.6 MeV and (b) for the isoscalar 2^+ state at 4.439 MeV. Shown are the proton form factor F_L^c (—), the weak form factor $F_L^{c,w}$ (---), the transverse electric form factors $F_{L,L+1}^{te}$ (---) and $F_{L,L-1}^{te}$ (---) as well as their weak counterparts $F_{L,L+1}^{te,w}$ (---o---) and $F_{L,L-1}^{te,w}$ (---o---) for (a) $L = 1$ and (b) $L = 2$.

are very different.

The weak density ϱ_w entering into the potential A_w is calculated from the convolution of the point-like proton (ϱ_p) and neutron (ϱ_n) density distributions of ^{12}C as predicted by SkM* [37] with the proton (G_p^w) and neutron (G_n^w) weak form factors as in [6, 38, 39],

$$\varrho_w(\mathbf{r}) = \int d\mathbf{r}' [G_p^w(\mathbf{r}')\varrho_p(\mathbf{r} - \mathbf{r}') + G_n^w(\mathbf{r}')\varrho_n(\mathbf{r} - \mathbf{r}')] . \quad (3.6)$$

The latter ones can be written in terms of the electromagnetic form factors ($G_{n,p}^{\text{em}}$) and the weak charges of the neutron (Q_n^w) and the proton (Q_p^w) in the usual way,

$$G_p^w = Q_p^w G_p^{\text{em}} + Q_n^w G_n^{\text{em}} \quad (3.7)$$

$$G_n^w = Q_n^w G_p^{\text{em}} + Q_p^w G_n^{\text{em}} \quad (3.8)$$

where at tree level in the Standard Model

$$Q_p^w = 1 - 4 \sin^2 \theta_w \quad (3.9)$$

$$Q_n^w = -1 \quad (3.10)$$

and the weak charge of the nucleus with N neutrons and Z protons is accordingly [5]

$$Q_w^{N,Z} = NQ_n^w + ZQ_p^w = \int dr \varrho_w(r). \quad (3.11)$$

For the case of ^{12}C , this leads to a weak charge of -5.55 at tree level and to -5.51 taking into account universal radiative corrections to $Q_p^w = 0.0719 \pm 0.0045$ and $Q_n^w = -0.9890 \pm 0.0007$ [14]. The absolute value of ϱ_w for ^{12}C is depicted in Fig. 2. Due to the fact that it is an $N = Z$ nucleus, the neutron and proton densities are very similar and thus, as can be seen, the electric and weak charge density distributions are also very similar in magnitude but have opposite signs. While our calculations are performed with $Q_w^{N,Z} = -5.51$, a renormalization by a factor $5.55/5.50$ reduces A_{pv} by up to 5% at a collision energy of 155 MeV and angles up to 175° .

The influence of ϱ_0 on the spin asymmetry A_{pv} is displayed in Fig. 4. The deviations are larger than for the differential cross section, particularly in the region of the diffraction minimum where A_{pv} shows a large oscillatory structure (Fig. 4b). Beyond the diffraction minimum even the shape of the energy distribution differs strongly. This sensitivity to the model densities at higher momentum transfers has to be kept in mind as a much larger source of uncertainty than the radiative corrections. In the subsequent calculations the Gaussian representation of the ground-state charge density is used.

Concerning the dispersive corrections, we have considered the most relevant excited states with angular momentum $L \leq 3$ and excitation energy $\omega_L < 30$ MeV as predicted by the SkM* effective interaction [37] solved via the Hartree-Fock plus Random Phase Approximation [27]. The six selected excited states are: three 1^- states at 19.6 (isovector), 20.9 (isoscalar) and 27.8 MeV (isoscalar); two 2^+ states at 4.439 (isoscalar) and 9.84 MeV (isovector); and one 3^- state at 9.64 MeV (isoscalar). The proton and neutron transition densities are calculated consistently within the same nuclear model. The corresponding form factors together with their weak counterparts are displayed in Fig. 5 for the 19.6 MeV (1^-) and the 4.439 MeV (2^+) state. The isoscalar states are characterized by a large weak charge form factor (Fig. 5b), while for the isovector states the magnetic weak form factors gain importance (Fig. 5a).

The influence of the radiative effects on the weak spin asymmetry is shown in Fig. 6 at a forward and a backward scattering angle. At small angles, dispersion is negligible as compared to the QED perturbation (Fig. 6a), while near and above the diffraction minimum, accessible at the larger angles, dispersion is dominating (Fig. 6b).

Let us now consider the relative changes by the QED effects (dA_{pv}^{QED}) and by dispersion (dA_{pv}^{box}). Their energy

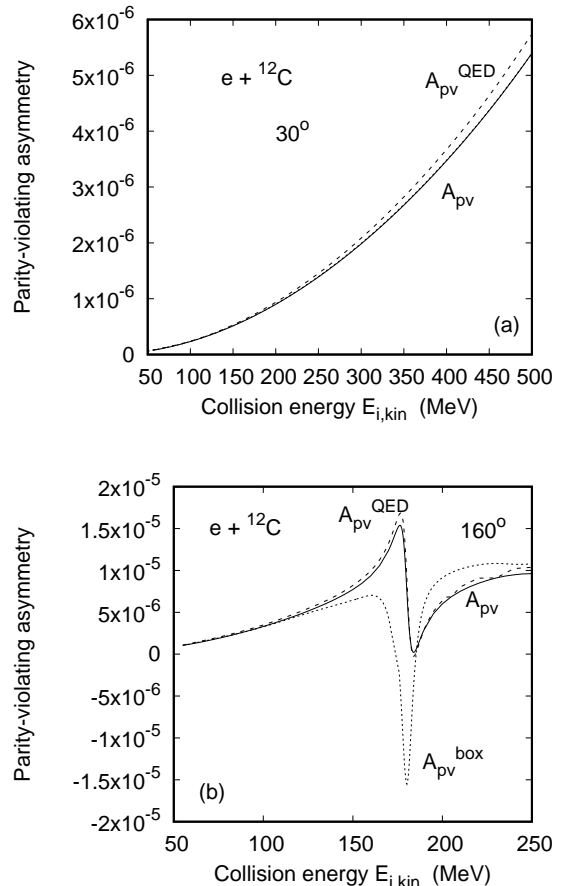


FIG. 6: Parity-violating asymmetry A_{pv} (—) in $e+^{12}\text{C}$ collisions, corrected for QED effects (A_{pv}^{QED} , - - -) and for dispersion (A_{pv}^{box} , ·····) (a) at 30° and (b) at 160° as function of collision energy.

distribution at 30° is displayed in Fig. 7. It is seen that both radiative effects vanish when the collision energy $E_{i,\text{kin}} = E_i - c^2$ tends to zero. In Fig. 7a the separate dispersion results are shown for the 19.6 and 27.8 MeV dipole, the 4.439 MeV quadrupole and the 9.64 MeV octupole excitation (whereas the 20.9 MeV and the 9.84 MeV contributions can be neglected). It follows that the main contribution to dispersion is due to the lowest quadrupole excitation, while the dipole states are of minor importance. This is opposite to the results found for the Sherman function where dispersion originates predominantly from the dipole states. The present result can be understood in terms of the form factors (Fig. 5). While for the 2^+ state the weak charge form factor is enhanced by a factor of two as compared to F_L^c , it is reduced by a factor of three in the case of the 1^- state. Also the magnetic weak form factors for this state are smaller than their protonic counterparts. We note that the above-mentioned renormalization of ϱ_w (by the factor $5.55/5.50$) changes $\Delta A_{pv}^{\text{box}}$ by at most 0.1%.

The correction of A_{pv} by the QED effects (Fig. 7b)

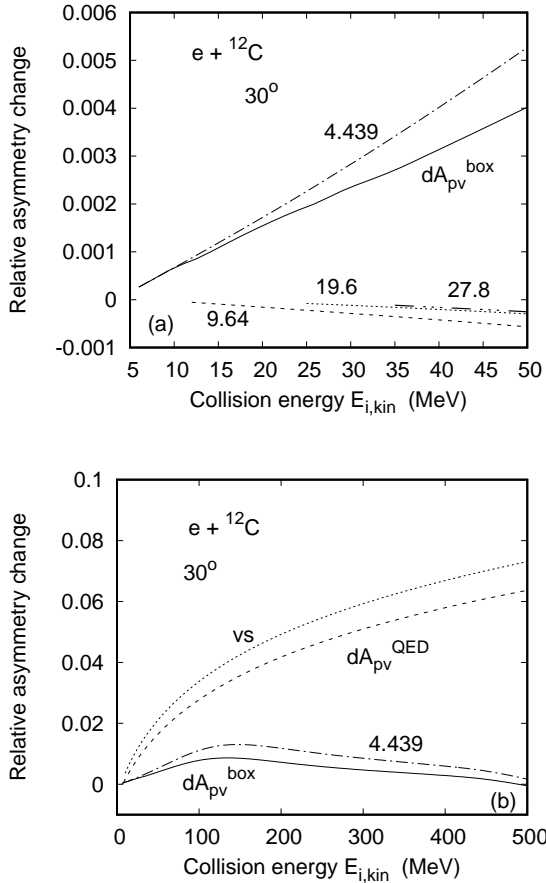


FIG. 7: Relative asymmetry change dA_{pv} in $e + {}^{12}\text{C}$ collisions at $\theta = 30^\circ$ as function of collision energy. Shown is $dA_{\text{pv}}^{\text{box}}$ (summed over all excited states, —) and $dA_{\text{pv}}^{\text{box}}(L, \omega_L)$ for the 2^+ state at 4.439 MeV (---). Included in (a) is $dA_{\text{pv}}^{\text{box}}(L, \omega_L)$ for the 3^- state at 9.64 MeV (----) and for the 1^- states at 19.6 MeV (.....) and 27.8 MeV (-·-·-). In (b), the change by the vertex plus self-energy correction (.....) and by both QED effects ($dA_{\text{pv}}^{\text{QED}}$, - - - -) is shown in addition.

is much larger than dispersion at this forward angle. The situation is, however, reversed at backward angles, which is shown for 160° in Fig. 8. Due to the diffraction oscillations of A_{pv} at this angle, where the weak spin asymmetry nearly vanishes, the definition of the relative spin asymmetry change is no longer meaningful. Therefore, the spin asymmetry modifications $\Delta A_{\text{pv}}^{\text{box}}$ and $\Delta A_{\text{pv}}^{\text{QED}}$ from (3.1) are displayed instead. The figure indicates that dispersion is nearly exclusively due to the lowest quadrupole state, showing a large excursion near the location of the diffraction minimum. The contribution from dipole and octupole states mostly cancel each other, even for still higher energies.

The angular distribution of the relative radiative changes for the two energies of 55 and 155 MeV is depicted in Fig. 9. While the QED effects are largely dom-

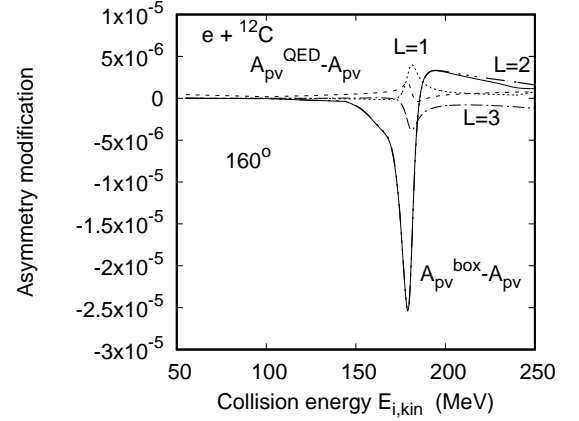


FIG. 8: Spin asymmetry modification ΔA_{pv} for electrons colliding with ${}^{12}\text{C}$ at 160° as function of collision energy. Shown are the dispersive modifications $\Delta A_{\text{pv}}^{\text{box}} = A_{\text{pv}}^{\text{box}} - A_{\text{pv}}$ when summed over the dipole states (.....), over the quadrupole states (-·-·-·-·-·-), over the octupole states (- - - -) as well as over $L \leq 3$ (———). Included is the asymmetry modification by the QED effects, $\Delta A_{\text{pv}}^{\text{QED}} = A_{\text{pv}}^{\text{QED}} - A_{\text{pv}}$ (- - - -).

inating at 55 MeV for all angles (Fig. 9a), there is a cross-over between $dA_{\text{pv}}^{\text{QED}}$ and $|dA_{\text{pv}}^{\text{box}}|$ near 130° at the higher energy (Fig. 9b).

We have also studied the radiative corrections in the high-energy regime. As a test case we have considered an energy of 953 MeV and a scattering angle of 4.7° , a geometry which has been selected for A_{pv} precision experiments on the lead nucleus [1]. For A_{pv} , being equal to 5.033×10^{-7} , the relative change by the QED effects is $dA_{\text{pv}}^{\text{QED}} = 3.64\%$ and by dispersion $dA_{\text{pv}}^{\text{box}} = -0.19\%$. Thus the dispersive effects from low-lying excited states can safely be neglected at such geometries and incident electron energies.

3.2. The ${}^{208}\text{Pb}$ nucleus

Like for the carbon nucleus, a Gaussian parametrization [40] of the experimentally determined nuclear ground-state charge distribution ϱ_0 is employed in the subsequent calculations. A comparison with the Fourier-Bessel charge distribution [40] shows a basic agreement except for very small nuclear distances as seen in Fig. 10. In contrast, the numerically obtained ϱ_0 from the nuclear model SkP [42] deviates from the Gaussian ϱ_0 in large regions of space. The effect of these deviations on the differential cross section for elastic scattering is negligibly small, as displayed in Fig. 3a for a collision energy of 155 MeV, except at the larger angles. The weak density for ${}^{208}\text{Pb}$, normalized to $Q_w = -118.76$ (which includes the universal radiative corrections [14]), is also shown in Fig. 10, again with a global minus sign for the sake of shape comparison. In contrast to the results for ${}^{12}\text{C}$, the absolute value of ϱ_w is about 30% higher than ϱ_0 for $R_N \lesssim 5$ fm, and even more in the outer region due to the

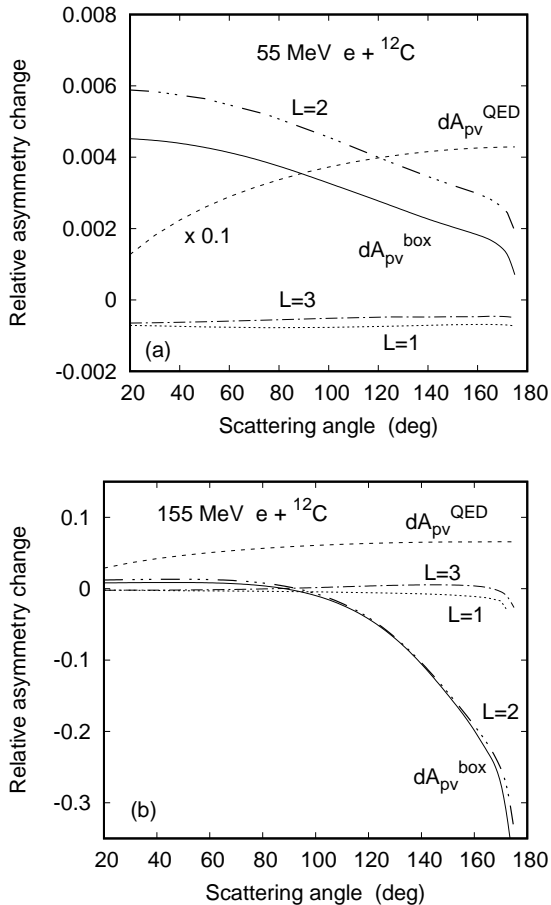


FIG. 9: Relative asymmetry change dA_{pv} in $e+^{12}\text{C}$ collisions (a) at 55 MeV and (b) at 155 MeV as function of scattering angle θ . Shown are the dispersive changes dA_{pv}^{box} when summed over the dipole states ($\cdots\cdots$), over the quadrupole states ($-\cdots-\cdots$), over the octupole states ($-\cdots-\cdots$) as well as over $L \leq 3$ (—). Included is the change dA_{pv}^{QED} by the QED effects ($-\cdots-\cdots$, reduced in (a) by the factor 0.1).

large neutron skin of the lead nucleus.

In order to account for dispersion, 10 dominant excited states with $L \leq 3$ and $\omega_L < 30$ MeV are considered. These are the five 1^- states at energies 5.512 MeV (isoscalar), and at 12.6, 14.3, 14.6 and 15.3 MeV (isovector). In addition, the three quadrupole states at 4.085 and 10.9 MeV (isoscalar) and at 21.6 MeV (isovector), as well as two octupole states at 2.615 MeV (isoscalar) and 27.9 MeV (isovector) are included. They are consistently calculated from the same (SkP) model [42]. It turns out that the most important ones are the 10.9 MeV 2^+ and the 2.615 MeV 3^- states. Their transition form factors are given in Fig. 11, together with the corresponding weak form factors. It is seen that for both states the weak charge form factors ($F_L^{c,w}$) are about a factor of two larger than the corresponding proton form factors (F_L^c). Like for the isoscalar states of ^{12}C , the magnetic form

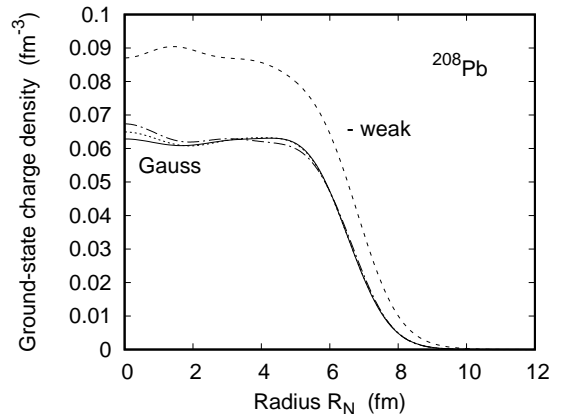


FIG. 10: Ground-state charge density ρ_0 of ^{208}Pb as function of the distance from the nuclear center. Shown are the Gaussian parametrization (—), the Fourier-Bessel fit ($\cdots\cdots$) and the result from the nuclear model ($-\cdots-$). Included is the negative of the weak density ρ_w ($-\cdots-$).

factors are much smaller, particularly for the 2.615 MeV state. For the sake of comparison, the form factors of the most relevant of the dipole states, the one at 14.3 MeV, are also shown (Fig. 11a). For all isovector 1^- states, proton and weak form factors have basically the same shape (but opposite sign).

The parity-violating spin asymmetry together with its radiative corrections is shown in Fig. 12. The angular distribution of A_{pv} at 155 MeV (Fig. 12a) exhibits an oscillatory behaviour in concord with the diffraction structures of the differential cross section (see Fig. 3a) which, however, are quite shallow. The QED effects enhance the spin asymmetry, particularly in the backward hemisphere. Also dispersion increases the spin asymmetry, well below 1% for $\theta < 60^\circ$, but up to 10% for the backward angles. The combined effect of both types of radiative corrections leads to a notable increase of A_{pv} , ranging from a few percent at forward angles to 20% at angles beyond 150° for this collision energy.

The behaviour of A_{pv} and its radiative corrections with energy is displayed in Fig. 12b for the forward scattering angle of 30° . The energy dependence of the diffraction structures is much alike their angular dependence, confirming that A_{pv} is basically dependent on momentum transfer which increases in a similar way with angle and with energy.

Again the radiative corrections enhance the weak spin asymmetry. The QED effects prevail, while dispersion is unimportant at this angle except for energies above 300 MeV.

Fig. 13 shows the relative change of A_{pv} by the radiative corrections at 155 MeV. For dispersion (Fig. 13a), the dominant contribution at the larger angles originates from the $L = 2$ and $L = 3$ excited states, with the 2.615 MeV state prevailing beyond 140° . The dipole states determine the angular distribution only at angles below 60° , and this basically because the quadrupole and octupole contributions cancel each other in this angular region.

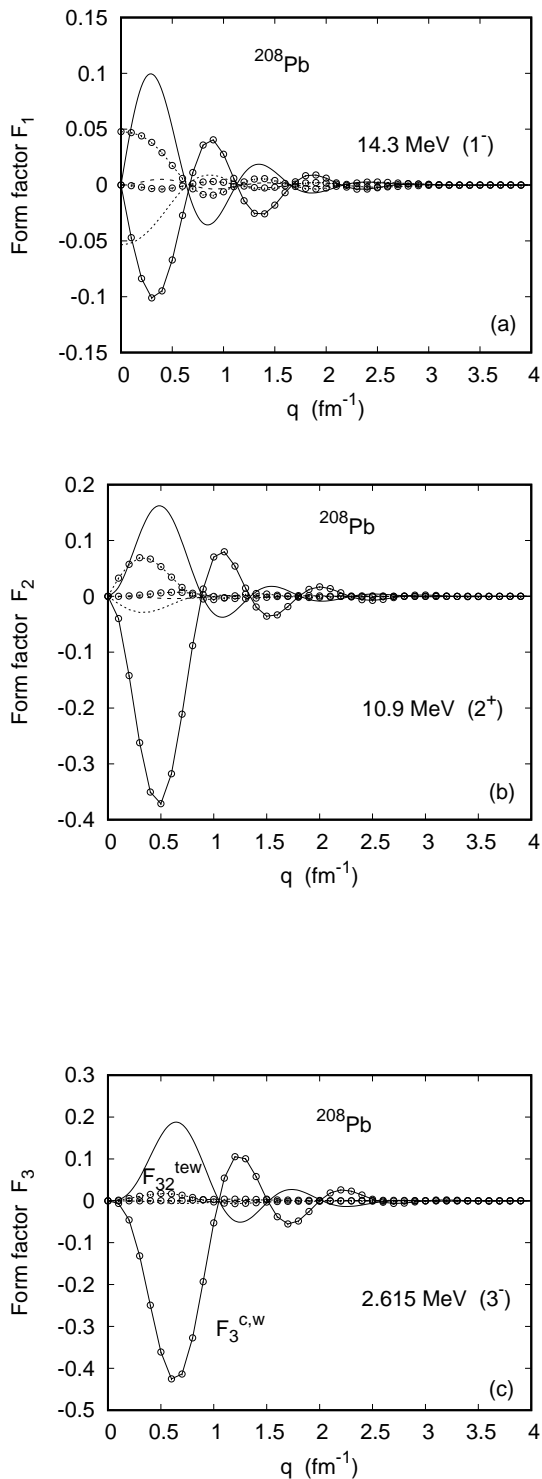


FIG. 11: Form factors as function of momentum transfer, (a) for the ^{208}Pb isovector 1^- state at 14.3 MeV, (b) for the isoscalar 2^+ state at 10.9 MeV and (c) for the isoscalar 3^- state at 2.615 MeV. Shown are the proton form factor F_L^c (—), the weak form factor $F_L^{c,w}$ (—○—), the transverse electric form factors $F_{L,L+1}^{te}$ (---) and $F_{L,L-1}^{te}$ (·····) as well as their weak counterparts $F_{L,L+1}^{te,w}$ (---○---) and $F_{L,L-1}^{te,w}$ (·····○·····) for (a) $L = 1$, (b) $L = 2$ and (c) $L = 3$.

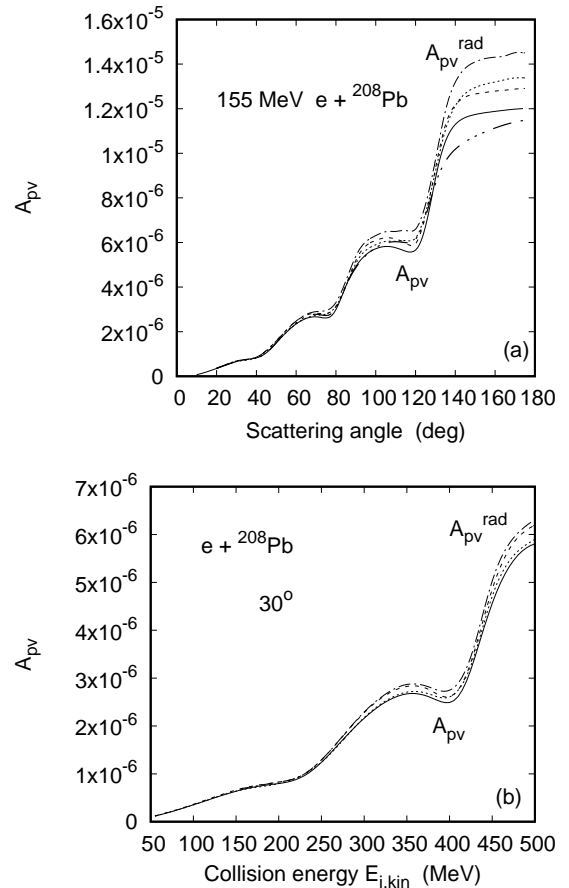


FIG. 12: Parity-violating asymmetry A_{pv} (—) in $e+^{208}\text{Pb}$ collisions, corrected for QED effects (A_{pv}^{QED} , ----) and for dispersion (A_{pv}^{box} , ·····) (a) at 155 MeV as function of scattering angle θ and (b) at 30° as function of collision energy $E_{i,\text{kin}}$. Included is the spin asymmetry corrected for both radiative effects (A_{pv}^{rad} , - · - · -).

The comparison with the QED corrections (Fig. 13b) reveals their dominance for $\theta \lesssim 100^\circ$, while dispersion catches up at the higher angles. The structures seen in the angular distribution are conform with the oscillations of A_{pv} (Fig. 12a). Each minimum in $\frac{d\sigma_{\text{count}}}{d\Omega}$ or in A_{pv} produces a large excursion of both dA_{pv}^{QED} and dA_{pv}^{box} . Included in Fig. 13b are the two constituents of dA_{pv}^{QED} , the change by vacuum polarization (amounting to about 1%) and by the vs correction which is of opposite sign and largely dominating.

The energy distribution of the relative spin asymmetry change is provided in Fig. 14 for a forward scattering angle. The dispersive corrections (Fig. 14a) are well below 1% at energies below 300 MeV. However, in contrast to ^{12}C at this angle (Fig. 7), they increase with energy, showing a maximum of about 5% in the second diffraction minimum, basically produced by the two isoscalar 2^+ excitations. The QED corrections (Fig. 14b) are largely

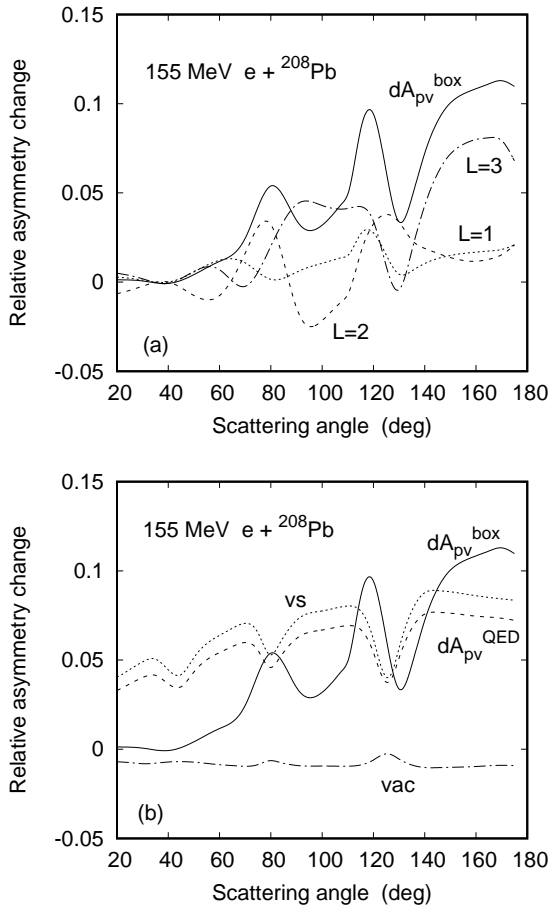


FIG. 13: Relative spin asymmetry change dA_{pv} in 155 MeV $e+^{208}\text{Pb}$ collisions as function of scattering angle θ . Shown in (a) are the dispersive changes dA_{pv}^{box} when summed over the dipole states (\cdots), over the quadrupole states ($---$), over the octupole states ($-\cdot-\cdot-$) and over all states with $L \leq 3$ (dA_{pv}^{box} , $---$). Shown in (b) are the QED changes by vacuum polarization ($---$), by the vertex plus self-energy correction (\cdots) and by both QED effects (dA_{pv}^{QED} , $-\cdot-\cdot-$). Included is dA_{pv}^{box} ($---$) from (a).

dominating at this angle, but near 400 MeV dispersion is nearly as large, resulting in a combined effect of 10%.

For the high-energy geometry, 953 MeV at 4.7° , our results are $A_{pv} = 5.896 \times 10^{-7}$, $dA_{pv}^{\text{QED}} = 3.93 \times 10^{-2}$ and $dA_{pv}^{\text{box}} = -1.07 \times 10^{-3}$, confirming that dispersion is negligible at small angles.

4. CONCLUSION

We have estimated the radiative corrections to the parity-violating spin asymmetry for electron scattering from ^{12}C and ^{208}Pb nuclei by treating the QED effects nonperturbatively and by estimating the dispersive corrections from low-lying excited states by evaluating the γZ box diagrams in second-order Born approximation.

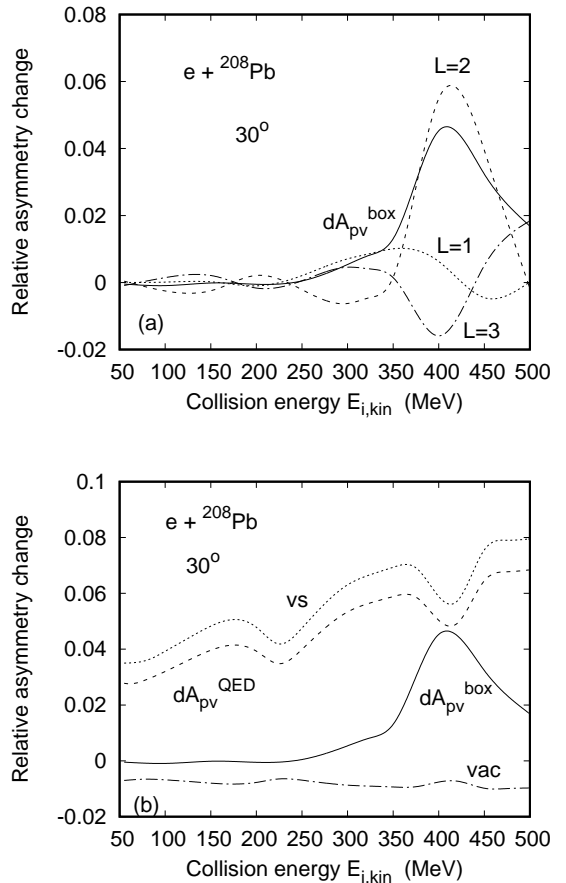


FIG. 14: Relative spin asymmetry change dA_{pv} in $e+^{208}\text{Pb}$ collisions at $\theta = 30^\circ$ as function of collision energy. Shown in (a) are the dispersive changes dA_{pv}^{box} when summed over the dipole states (\cdots), over the quadrupole states ($---$), over the octupole states ($-\cdot-\cdot-$) and over all states with $L \leq 3$ (dA_{pv}^{box} , $---$). Shown in (b) are the QED changes by vacuum polarization ($---$), by the vertex plus self-energy correction (\cdots) and by both QED effects (dA_{pv}^{QED} , $-\cdot-\cdot-$). Included is dA_{pv}^{box} ($---$) from (a).

We have found that at small scattering angles, irrespective of collision energy, the dispersive changes of A_{pv} are far less important than those by the QED effects.

At backward angles, on the other hand, dispersion is dominating and may affect A_{pv} by more than 10% at a collision energy of 155 MeV. In general it will be large in the diffraction minima of A_{pv} . For carbon, when the diffraction effects do not obscure the energy dependence of the spin asymmetry, we have found that dispersion decreases with energy beyond 150 MeV at forward angles. This is in concord with the expectation that the contribution from the low-lying excited states is suppressed according to $1/E_i^2$ for energies well above the pion production threshold [43]. On the other hand, the QED corrections are nearly independent of collision energy, amounting to a few percent [24]. A test study at 953 MeV

and 4.7° , the geometry selected in [1], leads to the suppression of dispersion as compared to the QED effects by $dA_{\text{pv}}^{\text{box}}/dA_{\text{pv}}^{\text{QED}} = -5.22 \times 10^{-2}$ for ^{12}C and -2.7×10^{-2} for ^{208}Pb . For the design of precision experiments it is important to choose small scattering angles, well below the onset of the diffraction structures. One reason is that the radiative corrections, calculated within a given nuclear model, are tiny at small angles but increase with angle, the more so the higher the collision energy. Moreover, also the dependence of the ground-state charge density and of the parity-violating asymmetry on the underlying nuclear models is quite strong for the larger angles. Also, whenever dispersion is important, the model-dependence of the transition densities cannot be neglected.

Acknowledgments

It is a pleasure to thank A.V.Afanasev and M.Gorshteyn for many enlightening discussions. X.R.M. acknowledges support by MICIU/AEI/10.13039/501100011033 and by FEDER UE through grants PID2023-147112NB-C22; and through the “Unit of Excellence Maria de Maeztu 2025–2028” award to the Institute of Cosmos Sciences, grant CEX2024-001451-M. Additional support is provided by the Generalitat de Catalunya (AGAUR) through grant 2021SGR01095.

-
- [1] D.Adhikari et al. (PREX Collaboration), Phys. Rev. Lett. **126**, 172502 (2021).
- [2] D.Adhikari et al. (CREX Collaboration), Phys. Rev. Lett. **129**, 042501 (2022).
- [3] D.Androić et al. (Qweak Collaboration), Phys. Rev. Lett. **128**, 132501 (2022).
- [4] S. Abrahamyan et al. (PREX Collaboration), Phys. Rev. Lett. **108**, 112502 (2012).
- [5] C.J.Horowitz, Phys. Rev. C **57**, 3430 (1998).
- [6] C. J. Horowitz, S. J. Pollock, P. A. Souder and R. Michaels, Phys. Rev. C **63**, 025501 (2001).
- [7] P.-G.Reinhard, X.Roca-Maza and W.Nazarewicz, Phys. Rev. Lett. **127**, 232501 (2021).
- [8] T.W.Donnelly, J.Dubach and I.Sick, Nucl. Phys. A **503**, 589 (1989).
- [9] C.J.Horowitz et al., Phys. Rev. C **85**, 032501(R) (2012).
- [10] M. Cadeddu, N. Cargioli, J. Erler, M. Gorchtein, J. Piekarewicz, X. Roca-Maza and H. Spiesberger, Phys. Rev. C **110** 035501 (2024).
- [11] M.Gorchtein and C.J.Horowitz, Phys. Rev. Lett. **102**, 091806 (2009).
- [12] M. Gorchtein, C. J. Horowitz, and M. J. Ramsey-Musolf, Phys. Rev. C **84**, 015502 (2011).
- [13] O.Koshchii, J.Erler, M.Gorchtein, C.J.Horowitz, J.Piekarewicz, X.Roca-Maza, C.-Y.Seng and H.Spiesberger, Phys. Rev. C **102**, 022501 (2020).
- [14] S. Navas *et al.* (Particle Data Group Collaboration) Phys. Rev. D **110**, 030001 (2024).
- [15] J.L.Friar and M.Rosen, Ann. Phys. **87**, 289 (1974).
- [16] D.H.Jakubassa-Amundsen, Phys. Rev. C **105**, 054303 (2022).
- [17] A.V.Afanasev and N.P.Merenkov, Phys. Lett. B **599**, 48 (2004); arXiv:0407167v2 (2005)
- [18] M.Gorchtein and C.J.Horowitz, Phys. Rev. C **77**, 044606 (2008).
- [19] O.Koshchii, M.Gorchtein, X.Roca-Maza and H.Spiesberger, Phys. Rev. C **103**, 064316 (2021).
- [20] N.L.Hall, P.G.Blunden, W.Melnitchouk, A.W.Thomas and R.D.Young, Phys. Lett. B **731**, 287 (2014).
- [21] K.Aulenbacher, Hyperfine Interact **200**, 3 (2011).
- [22] E.A.Uehling, Phys. Rev. **48**, 55 (1935).
- [23] D.H.Jakubassa-Amundsen, J. Phys. G **51**, 035105 (2024).
- [24] X. Roca-Maza and D. H. Jakubassa-Amundsen, Phys. Rev. Lett. **134**, 192501 (2025).
- [25] Energy Density Functional Methods for Atomic Nuclei, ed. N. Schunck (IOP, Bristol, 2019).
- [26] G.Colò, L.-G.Cao, N. Van Giai and L.Capelli, Comp. Phys. Commun. **184**, 142 (2013).
- [27] G.Colò and X. Roca-Maza arXiv: 2102.06562 (2021).
- [28] T.W.Donnelly and I.Sick, Rev. Mod. Phys. **56**, 461 (1984).
- [29] L.W.Fullerton and G.A.Rinker Jr., Phys. Rev. A **13**, 1283 (1976).
- [30] Y.S.Tsai, Phys. Rev. **120**, 269 (1960).
- [31] M.Vanderhaeghen, J.M.Friedrich, D.Lhuillier, D.Marchand, L.Van Hoorebeke, J.Van de Wiele, Phys. Rev. C **62**, 025501 (2000).
- [32] M.Thomson, *Modern Particle Physics* (Cambridge University Press, Cambridge, 2013).
- [33] C.J.Horowitz and J.Piekarewicz, Phys. Rev. C **86**, 045503 (2012).
- [34] J.W.Motz, H.Olsen and H.W.Koch, Rev. Mod. Phys. **36**, 881 (1964).
- [35] A.Goldberg, Il Nuovo Cimento **20**, 1191 (1961).
- [36] F.Salvat, J.M.Fernández-Varea and W.Williamson Jr., Comput. Phys. Commun. **90**, 151 (1995).
- [37] J. Bartel, P. Quentin, M. Brack, C. Guet, and H.-B. Hakansson, Nucl. Phys. A **386**, 79 (1982)
- [38] X. Roca-Maza, M. Centelles, X. Viñas, M. Warda, Phys.Rev.Lett. **106** (2011) 252501.
- [39] Paul-Gerhard Reinhard, Xavier Roca-Maza, Witold Nazarewicz, Phys. Rev. Lett. **127**, 232501 (2021)
- [40] H.De Vries, C.W.De Jager and C.De Vries, At. Data Nucl. Data Tables **36**, 495 (1987).
- [41] V.B.Berestetskii, E.M.Lifshitz and L.P.Pitaevskii, *Quantum Electrodynamics* (Course of Theoretical Physics vol.4) 2nd edition (Elsevier, Oxford, 1982).
- [42] J.Dobaczewski, H. Flocard, and J. Treiner, Nucl. Phys. A **422**, 103 (1984).
- [43] M.Gorshteyn, Private Communication (2024).